

A new X-ray nova MAXI J1910–057 (= Swift J1910.2–0546) and mass-accretion inflow

Satoshi NAKAHIRA¹, Hitoshi NEGORO², Megumi SHIDATSU³, Yoshihiro UEDA³,
 Tatehiro MIHARA⁴, Mutsumi SUGIZAKI⁴, Masaru MATSUOKA⁴ and Takuya ONODERA²

¹*ISS Science Project Office, Institute of Space and Astronautical Science (ISAS), Japan Aerospace Exploration Agency (JAXA), 2-1-1 Sengen,
 Tsukuba, Ibaraki 305-8505*

²*Department of Physics, Nihon University, 1-8-14, Kanda-Surugadai, Chiyoda-ku, Tokyo 101-8308*

³*Department of Astronomy, Kyoto University, Oiwake-cho, Sakyo-ku, Kyoto 606-8502*

⁴*MAXI team, Institute of Physical and Chemical Research (RIKEN), 2-1 Hirosawa, Wako, Saitama 351-0198*

(Received $\langle \rangle$; accepted $\langle \rangle$)

Abstract

We report on a long-term monitoring of a newly discovered X-ray nova, MAXI J1910–057 (= Swift J1910.2–0546), by MAXI and Swift. The new X-ray transient was first detected on 2012 May 31 by MAXI Gas Slit Camera (GSC) and Swift Burst Alert Telescope (BAT) almost simultaneously. We analyzed X-ray and UV data for 270 days since the outburst onset taken by repeated MAXI scans and Swift pointing observations. The obtained X-ray light curve for the initial 90 days is roughly represented by a fast-rise and exponential-decay profile. However, it re-brightened on the ~ 110 days after the onset and finally went down below both GSC and BAT detection limits on the 240 day. All the X-ray energy spectra are fitted well with a model consisting of a multi-color-disk blackbody and its Comptonized hard tail. During the soft-state periods, the inner-disk radius of the best-fit model were almost constant. If the radius represents the innermost stable circular orbit of a non-spinning black hole and the soft-to-hard transitions occur at 1–4% of the Eddington luminosity, the mass of the compact object is estimated to be $> 2.9M_{\odot}$ and the distance to be > 1.70 kpc. The inner-disk radius became larger in the hard / hard-intermediate state. This suggests that the accretion disk would be truncated. We detected an excess of the UV flux over the disk blackbody component extrapolated from the X-ray data, which can be modelled as reprocessed emission irradiated by the inner disk. We also found that the UV light curve mostly traced the X-ray curve, but a short dipping event was observed in both the UV and the X-ray bands with a 3.5-day X-ray time lag. This can be interpreted as the radial inflow of accreting matter from the outer UV region to the inner X-ray region.

Key words: accretion disks — black hole physics — stars: individual (MAXI J1910–057) — X-rays: stars

1. Introduction

Galactic low-mass X-ray binaries (LMXBs) are classified into two different types, neutron star binary and black hole X-ray binary (BHXB). While some of LMXBs are persistently on, most of the BHXBs are thought to be transients that are normally in a quiescent state and occasionally exhibit episodic brightening called “outburst”. The outburst is triggered by sudden increase of mass accretion rate onto the compact star. There are two competing models that regulate the accretion flow, namely, “mass transfer instability model” (Hameury et al. 1994) and “disk thermal instability model” (Mineshige & Wheeler 1994).

During the outburst, BHXBs change its X-ray luminosity in several orders of magnitude and transit through two major spectral states, “soft state” and “hard state”. The X-ray spectrum in the soft state (hereafter SS) is characterized by an ultra-soft component which originates from optically-thick and geometrically-thin accretion disk, called “standard disk” (Shakura & Sunyaev 1973). Many observations show that the inner-most radius r_{in} remains constant irrespective of variation of the inner most temperature. Therefore, the r_{in} is believed to reflect the inner stable circular orbit (ISCO). The hard state (hereafter HS) is approximated by a single power-law with a

photon index 1.4–2.0 and a high-energy cutoff at ~ 100 keV. Sunyaev & Trümper (1979) successfully explained this emission by thermal Comptonization of soft seed photons in the hot corona. The seed photons are believed to come from the standard disk which is truncated in a large r_{in} (Zdziarski et al. 1998, Makishima et al. 2008). The hysteresis in X-ray intensity between the HS-to-SS and SS-to-HS state transitions produces a q-shaped track in a hardness intensity diagram, called “q-curve” (Homan & Belloni 2005).

Past X-ray observations of BHXBs including *RXTE* and MAXI revealed a variety of light-curve profiles among BHXBs (e.g. Chen et al. 1997). “X-ray nova” is a subclass of these BHXB transients, which includes A0620–00 (Kaluzienski et al. 1977), GS 1124–68 (Ebisawa et al. 1994), GS 2000+25 (Tsunemi et al. 1989) and GRO J0422+32 (Harmon et al. 1992). They are characterized by a simple light-curve profile of fast-rise and exponential-decay normally followed by late *re-flaring* (Tanaka & Shibazaki 1996). The simple profile allows us to study accretion inflow of the black-hole binary system apart from complicated behavior around the inner disk.

A newly discovered X-ray transient MAXI J1910–057 (= Swift J1910.2–0546) is categorized into X-ray novae from the profile of the X-ray light curve. The source was detected by Gas-Slit Camera (GSC; Mihara et al. 2011) on-

board Monitor All-sky X-ray Image (MAXI; Matsuoka et al. 2009) operated on the international space station (ISS). On 2012 May 31 22:36 (MJD=56078.941667), MAXI transient alert system (NovaSearch; Negoro et al. 2012) detected an enhanced X-ray emission at (R.A., Dec)=(287°8, −5°8), and then issued a flash report tagged by Trigger ID=6078777285 to the “New-transient” alert mailing list¹ maintained by MAXI team. The updated information was also reported to the Astronomer’s Telegram (Usui et al. 2012). Swift Burst Alert Telescope (BAT; Barthelmy et al. 2005) independently detected the source (Krimm et al. 2012). Therefore, this source is also referred to as Swift J1910.2–0546. The first Swift pointing observation, performed at 2012 June 1 14:41 (MJD 56079.611806), refined the source position to (R.A., Dec) (J2000) = (19^h10^m22^s.78, −05°47′58″.0) (Kennea et al. 2012) with an uncertainty of 3″.5 radius. The source is also identified with optical observations (Rau et al. 2012). Previous works on this source by Reis et al. (2013) presented results of two *XMM–Newton* observations in a hard or hard-intermediate state, and they reported a possibility of retrograde spin. Degenaar et al. (2014) investigated the correlation around the re-flare using multi wavelength light curves from near-infrared to X-ray bands.

In this paper we studied this “classical” X-ray nova from the onset on 2012 May 31 (MJD=56078) to the end of the activity around 2013 January 26 (MJD=56318) using data of MAXI and Swift, complementally. Hereafter, t denotes the elapsed time since the date of the onset, MJD=56078.0. We performed light-curve and spectral analyses of X-ray and UV data utilizing HEASOFT version 6.13 with xspec version 12.8.0m, and MAXI specific tools developed on the basis of ftools. Errors represent 1σ and 90% confidence limits for light curve data and best-fit spectral parameters, respectively, throughout the following sections.

2. Instruments and Data Reduction

2.1. MAXI

MAXI, in operation since 2009 August, has two scientific instruments, GSC and SSC (Solid-state Slit Camera; Tomida et al. 2011). Both GSC and SSC cover two instantaneous rectangular fields of view (FOV), aimed at the earth horizon and the zenith directions. Each FOV of $3 \times 160 \text{ deg}^2$ in GSC and $3 \times 90 \text{ deg}^2$ in SSC is determined by a slit and slats collimators. The target visibility is determined by an ISS attitude which rotates with the orbital motion. Each visible time (hereafter referred to as “transit”) lasts for 50–150 sec for GSC, and 40–60 sec for SSC. The effective area changes due to the triangular-shaped collimator transmission with a peak value of 4–5 and 0.6–0.9 cm^2 for GSC and SSC, respectively.

2.1.1. GSC data

We used MAXI specific analysis tools and the script which are developed by the MAXI team. These software are utilized in the MAXI on-demand data processing system accessed via web interface²(Nakahira et al. 2012), where the latest calibration information is applied. In the period of interest in this

paper, six GSC counters out of the twelve were turned on, and others were kept off for redundancy (Sugizaki et al. 2011). We utilized data of GSC #0, 2, 7 operated at the high voltage of 1550 V and of GSC #4, 5 at 1650 V. Here we did not utilize GSC#3 because it was degraded and not suitable for spectral analysis. The X-ray event data archived as the GSC event revision 1.4 was used. Then we set the source regions and the background regions for the analysis. For source regions, a circle centered at the target position was used. Because 1550 V counters have relatively wider PSF than those of 1650 V, we use the radius r_s of $2^\circ 0$ and $1^\circ 5$, respectively. For background regions we used an annulus region between an inner radius of $r_s + 0^\circ 1$ and an outer radius of $r_s + 1^\circ 0$ centered on the target position. Additionally we excluded X-ray events within $1^\circ 5$ from an X-ray burster 4U 1916–053 which locates $2^\circ 1$ apart from the target source. We discarded these data where the source and background regions 1) were shaded by solar panels or other ISS structure, or 2) the scan of either region was not completed. As a result, we collected 2886 transits of $493.6 \text{ cm}^2 \text{ ksec}$.

2.1.2. SSC data

The SSC observation was conducted in similar manner as GSC. Hence, SSC data is analyzed in the similar manner as the GSC except for the data screening. We first removed the hot pixels with `cleansis` in `ftools`. We then collected single-pixel events (G0) in the energy band below 1.84 keV, and included split events (G12) above 1.84 keV. The energy gain was corrected by using copper K_α emission line from the SSC camera body, and the gain temperature dependence was also corrected. Since the SSC data were contaminated by the visible/infrared light from the Sun and Moon (Tsunemi et al. 2010), we selected data taken during the ISS night time, and then eliminated such events that the angular separation from the Moon is $< 5^\circ$. In this manner, we collected 844 transits of $22.2 \text{ cm}^2 \text{ ks}$. To avoid thermal noise due to relatively higher CCD temperature, we ignored energy bin below 0.7 keV, above 7 keV dominated by background. Since the response function of SSC has calibration uncertainties of about 10% in normalization, we performed simultaneous model fits to both GSC and SSC spectral data introducing a cross normalization factor. We set the factor equal to 1.0 in GSC, and let free in SSC.

2.2. Swift

Since the discovery of the new X-ray source, MAXI J1910–057 (= Swift J1910.2–0546), Swift (Burrows et al. 2005) pointing observations were carried out with X-Ray Telescope (XRT) and UV Optical Telescope (UVOT; Roming et al. 2006) every one to \sim ten day interval. Due to the Sun angle constraint, no observations were available from 2012 November 26 to 2013 March 9. We utilized all the observation data taken until 2012 November, whose target IDs are 32480, 32521 and 32742.

2.2.1. XRT data

We utilized both data taken with PC and WT modes with an exposure of a few ks. All X-ray spectra and light-curve files were produced on the data-archive web site supplied by the UK Swift Science Data Centre at the University of Leicester (Evans et al. 2009). We performed spectral analysis with a response matrix file `swxwt0to2s6_20010101v014.rmf` in the 0.4–10 keV energy band.

¹ <https://maxi.riken.jp/mailman/listinfo/new-transient>

² <http://maxi.riken.jp/mxondem>

2.2.2. UVOT data

We collected UVOT data from NASA/HEASARC data center. We extracted fluxes and energy spectra with `uvotproduct` and `uvot2pha` in `ftools`, respectively. Since observations of ID=32521 were performed with a single UVM2 filter (2246 Å), the light curve analysis is focused on the UVM2 band. We integrated image using `uvotimsum`, and then estimated background carefully from the source free region.

2.2.3. BAT light curve

The Burst Alert Telescope (BAT) on Swift is an all-sky monitor to search for Gamma-ray bursts. While searching for bursts, it is capable of monitoring hard X-ray sources. We utilized the archived 15–50 keV light-curve data with a one-day time bin, available on the “BAT Transient Monitor” website (Krimm et al. 2013)³.

3. Analysis results

3.1. Light curves and hardness variations

In figure 1, we plot GSC 2–6 keV and 6–20 keV light curves and their hardness ratio (HR1), SSC 0.7–2 keV and 2–7 keV light curves, XRT 0.4–10 keV light curve and hardness ratio of the 5–10 keV to the 3–5 keV (HR2), UVOT light curve with UVM2 filter, and BAT 15–50 keV light curve. Data are binned by 0.5, 1, 2, 4 or 8 days depending on photon statistics of each bin. GSC scanned the source almost every day since the mission started in 2009 August. We investigated the GSC event data before the outburst onset. However, no significant excess over the background was detected. The hardness variation implies that the source exhibited spectral transition between HS and SS. Hence, we divided the entire periods into five intervals, labeled as HS1 ($t < 3$ d), SS1 ($3 \text{ d} < t < 66$ d), HS2 ($66 \text{ d} < t < 102$ d), SS2 ($102 \text{ d} < t < 132$ d), and HS3 ($132 \text{ d} < t$) in figure 1, according to the HR1 below/above 0.4, or HR2 below/above 0.2. We employed HR1 in $t < 80$ d and HR2 in $t > 80$ d according to the data frequency and the photon statistics.

As noticed from the GSC light curves, the 2–6 keV flux increased rapidly in the outburst beginning and reached the peak of $1.70 \text{ counts cm}^{-2} \text{ s}^{-1} \simeq 950 \text{ mCrab}$ at $t \sim 10$ d, where the 6–20 keV flux decreased. This caused the state transition from HS1 to SS1. While the X-ray emission in the soft state is dominated by a soft component, a weak hard X-ray peak was also seen at around $t = 15 - 30$ d (Kimura et al. 2012). In the SS1, the 2–6 keV flux declined steady, but the 6–20 keV turned to increase at $t = 50$ d, and then the source returned to the hard state (HS2) (Nakahira et al. 2012).

After $t \sim 100$ d, the source repeated the same state-change cycle of the hard(HS2)-soft(SS2)-hard(HS3) while the intensity declined gradually. In the HS3, the X-ray intensity varied to some degree keeping a hard spectrum. Further decay began around $t = 230$ d, and gone below both GSC and BAT detection limits after $t = 240$ d.

The UV light curve showed similar shape to soft X-ray light curve from SS1 until $t = 140$ d. However, it showed a clear deviation after then. The correlation between UV and X-ray is studied in section 3.4.

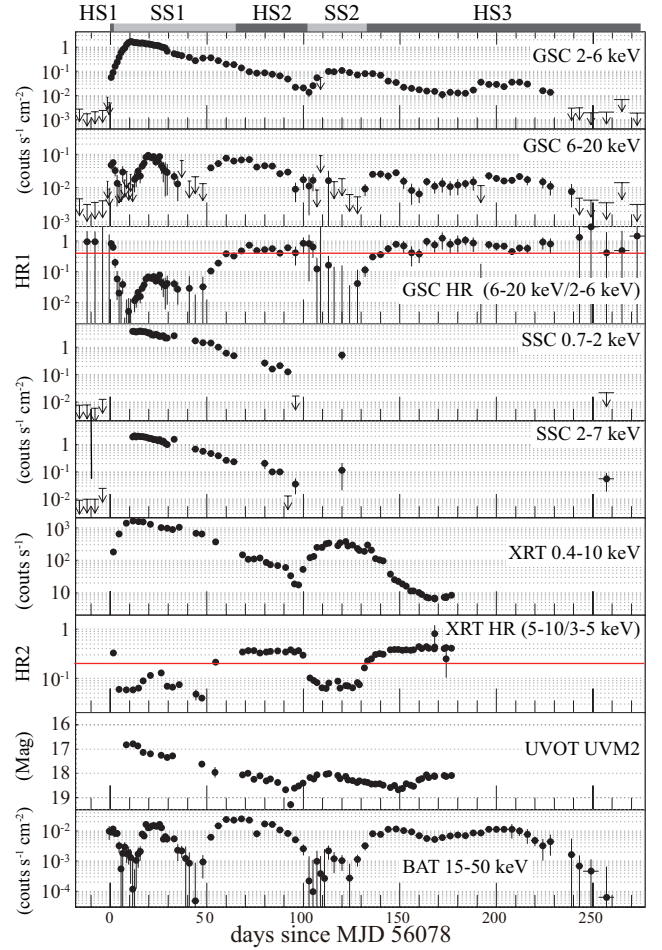


Fig. 1. Upper three panels are MAXI/GSC 2–6 keV, 6–20 keV counts and hardness ratio between 6–20 keV and 2–6 keV band (HR1). The next six panels show MAXI/SSC 0.7–2 keV and 2–7 keV lights curve, then Swift/XRT 0.4–10 keV, 5–10/3–5 keV (HR2), Swift/XRT light curve of UVM filter, and Swift/BAT 15–50 keV. Five periods split by MAXI/GSC HR=0.4 and Swift HR=0.2 (red lines) are shown at the top of the figure.

The entire structures of light curve is characterized with a fast rise and an exponential decay, followed by a re-flaring and latter long tail. This feature resembles the classical black hole X-ray novae (Tanaka & Shibazaki 1996).

3.2. Evolution of X-ray Spectrum

We investigate X-ray spectral evolution during the entire outburst using MAXI data with a continuous time coverage and Swift XRT data with a high sensitivity. Because daily MAXI data taken by GSC and SSC do not have enough photon statistics except for the initial bright phase, we accumulated spectral data for periods of several days for each of GSC and SSC. If both GSC and SSC data are available in some time period, they were fitted simultaneously. Swift XRT spectra were accumulated for each pointing observations. Figure 2 presents representative X-ray spectra in a νF_ν form.

Since the compact object is suggested to be a black hole from the light curve, we employed a model consisting of a Multi-Color Disk-blackbody (MCD; Mitsuda et al. 1984),

³ <http://swift.gsfc.nasa.gov/docs/swift/results/transients>

diskbb in *xspec* terminology, and its Compton up-scattered component with hot thermal electrons, *nthcomp*. To account for an interstellar absorption, we applied the Tuebingen-Boulder ISM absorption model (*TBabs*) with an abundance model of Wilms et al. (2000). The model is described by $TBabs \times (diskbb + nthcomp)$ with free parameters of the neutral hydrogen column density (N_H), innermost temperature (T_{in}) and normalization of the *diskbb*, photon index (Γ), electron temperature (kT_e) and a normalization of the *nthcomp*. We fixed kT_e at 50 keV because it cannot be constrained in the observed X-ray band. Since some observations in the bright phases indicated edge-like residuals between data and model probably due to error in the response function, we assigned systematic error of 5% into each energy bin corresponds 1.6–2.2 keV of the spectra.

Firstly, we fitted the model to all extracted XRT spectra allowing N_H free. The best-fit N_H values were mostly consistent with $0.41 \times 10^{22} \text{ cm}^{-2}$ during the soft-state periods (SS1 and SS2). In the hard state, the value could not be constrained because the soft X-ray continuum is not well determined. Hence, we adopted the best-fit N_H in the soft state, $0.41 \times 10^{22} \text{ cm}^{-2}$, as the intrinsic interstellar absorption. In the SS, Γ cannot be determined for each spectrum due to the limited effective area of GSC, SSC and XRT in the higher energy band. Therefore, we fixed Γ at 2.4 as typical value in SS (McClintock & Remillard 2006), and we left Γ free in the HS. In some of the HS spectra observed by GSC alone, the direct MCD component represented by *diskbb* was not significantly detected due to the poor efficiency in the lower energy band. In this case, we removed *diskbb* and assigned the typical $T_{in}=0.15$ keV for a seed photon of *nthcomp*. We confirmed that the assumed T_{in} does not change the best-fit Γ in the 2–20 keV band.

The fits to all the extracted spectra were mostly acceptable. Table 1 summarizes the best-fit parameters for the representative spectra in figure 3, where the best-fit models are overlaid on the data. Assuming that the Compton up-scattering process is isotropic and preserves the number of photons, we estimated innermost radius r_{in} of the MCD model with a following equation (Kubota et al. 2004)

$$F_{\text{disk}}^p + F_{\text{thc}}^p 2 \cos i = 0.0165 \left[\frac{r_{in}^2 \cos i}{(D/10 \text{ kpc})^2} \right] \left(\frac{T_{in}}{1 \text{ keV}} \right)^3 \text{ photons s}^{-1} \text{cm}^{-2} \quad (1)$$

where the F_{disk}^p and F_{thc}^p represent the photon fluxes from the MCD and Comptonized component, respectively. We also calculated the fraction of the Compton-scattered photon, $f_{sc} = \frac{F_{\text{thc}}^p}{F_{\text{disk}}^p + F_{\text{thc}}^p}$. These values are listed in 1. Figure 3 shows the variations of the spectral parameters as a function of time.

3.3. X-ray hardness-intensity diagram

In order to clarify the spectral evolution, hardness-ratio versus flux diagrams were plotted in figure 4. The horizontal axis and vertical axis represent Swift/XRT 3–5/5–10 keV HR and F_X obtained with model fits, respectively. The figure is split into (a) HS1, SS2 and before $t=90$ d of HS2, (b) after $t=90$ d of HS2, SS2 and HS3. Comparing the diagram with those obtained with past observations of black holes (e.g. Homan & Belloni 2005, Nakahira et al. 2010), we found two un-

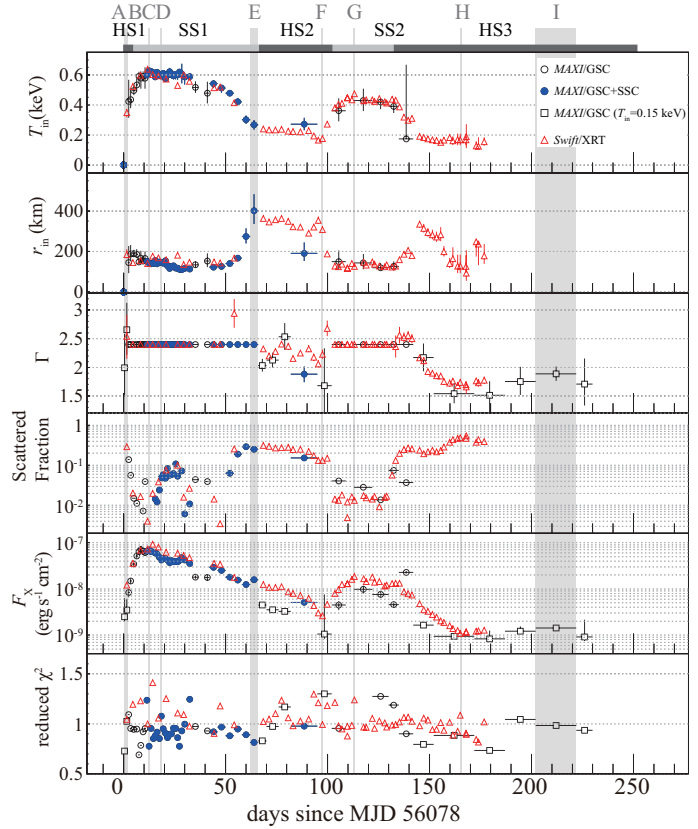


Fig. 3. Time evolution of spectral parameters derived from spectral fit. Circled points are MAXI/GSC (open black) and GSC plus SSC (filled blue) data analyzed with $TBabs \times (diskbb + nthcomp)$ model, and triangular points are those with Swift/XRT data. Square points show that with GSC data but $T_{in}=0.15$ keV is assumed. The panels from the top indicate, innermost temperature T_{in} (keV), innermost radius r_{in} , photon index Γ , fraction of *nthcomp* component, unabsorbed model flux in 0.01–100 keV F_X and reduced χ^2 . Time periods corresponding to HS1–3, SS1–2 and A–H in figure 2 are shown above.

usual features. One is that it exhibited hard-to-soft and soft-to-hard spectral state transitions twice, as seen in figures 4(a) and (b). The other is transition luminosities. Usually Hard-to-soft transition occurs at higher luminosity than soft-to-hard transition. However, in the case of SS2 to HS3 transition occurred at \sim twice brighter luminosity than that of HS2 to SS2 transition. Nevertheless, we found that SS1 to HS2 and SS2 to HS3 transitions occur at a similar X-ray flux. If we assume that the transitions occur at HR of 0.15–0.25, the corresponding flux becomes $1.28\text{--}2.33 \times 10^{-8} \text{ erg cm}^{-2} \text{ s}^{-1}$.

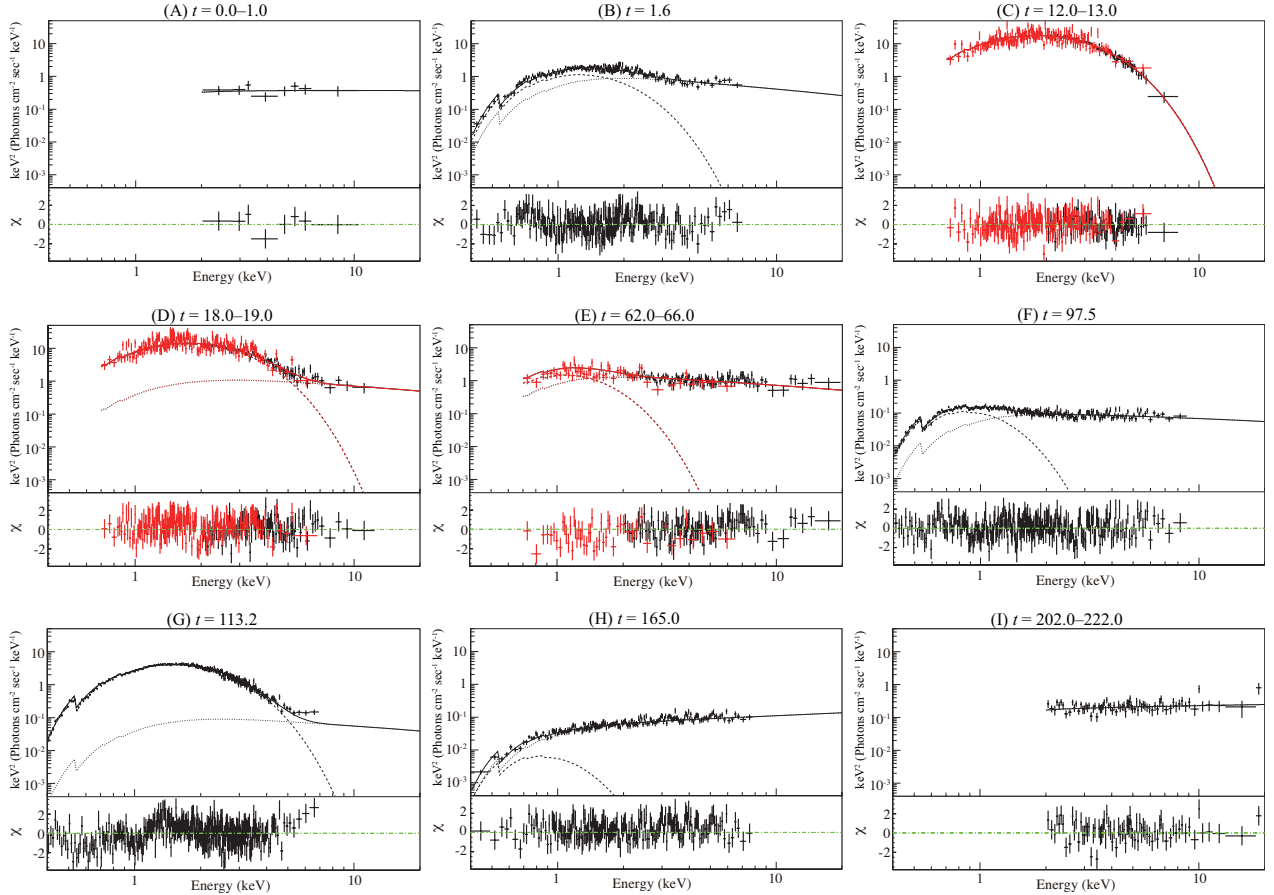
3.4. X-ray and UV correlation

In this section, we investigate relation between X-ray and UV emission. Since optical/UV emission is reddened by the dust lying in the line of sight toward the source, we estimated the extinction factor utilizing empirical relation given by Güver et al. (2009) as $N_H = (2.21 \pm 0.09) A_V \times 10^{21} \text{ cm}^{-2}$. From $N_H = 0.41 \times 10^{22} \text{ cm}^{-2}$ obtained by X-ray spectrum, and assuming $A_V = 3.1E(B - V)$ (Savage & Mathis 1979), we obtained $E(B - V) = 0.598$.

Table 1. Best-fit model parameters obtained from MAXI/GSC, SSC and Swift/XRT spectra.

Period	Instruments	t^* (day)	T_{in} (keV)	r_{in}^{\dagger} (km)	Γ	f_{sc}^{\ddagger}	F_X^{\S}	$\chi^2 / \text{d.o.f}$
A	MAXI/GSC	0.0–1.0	–	–	$1.99^{+0.59}_{-0.51}$	–	$5.0^{+16.7}_{-1.3}$	4.4 / 6
B	Swift/XRT	1.6	0.35 ± 0.03	183^{+29}_{-19}	$2.54^{+0.38}_{-0.39}$	0.30	$12.0^{+0.2}_{-0.3}$	214.9 / 201
C	MAXI/GSC+SSC	12.0–13.0	0.63 ± 0.01	$141.6^{+4.6}_{-4.2}$	2.4 (fixed)	0.00	69.1 ± 2.5	168.5 / 217
D	MAXI/GSC+SSC	18.0–19.0	0.59 ± 0.02	$146.4^{+5.9}_{-5.7}$	2.4 (fixed)	0.05	$66.4^{+3.7}_{-3.5}$	272.8 / 254
E	MAXI/GSC+SSC	62.0–66.0	0.27 ± 0.03	400^{+83}_{-64}	2.4 (fixed)	0.25	48.3 ± 1.8	116.2 / 143
F	Swift/XRT	97.5	0.18 ± 0.01	303^{+16}_{-14}	2.26 ± 0.08	0.14	2.6 ± 0.1	364.3 / 362
G	Swift/XRT	113.2	0.47 ± 0.00	125.8 ± 1.4	2.4 (fixed)	0.01	18.5 ± 0.1	480.3 / 388
H	Swift/XRT	165.0	0.17 ± 0.04	128^{+57}_{-35}	$1.73^{+0.06}_{-0.07}$	0.49	1.1 ± 0.1	386.6 / 356
I	MAXI/GSC	202.0–222.0	–	–	$1.88^{+0.13}_{-0.12}$	–	$2.5^{+0.3}_{-0.2}$	72.7 / 74

* Elapsed days since MJD=56078.0

 \dagger D=10.0 kpc and $i = 0$ are assumed. \ddagger Scattering fraction of the model, calculated from photon numbers of diskbb (F_{disk}^p) and nthcomp (F_{thc}^p) to be $\frac{F_{\text{thc}}^p}{F_{\text{thc}}^p + F_{\text{disk}}^p}$. \S Absorption-corrected model flux in units of $10^{-9} \text{ erg cm}^{-2} \text{ s}^{-1}$ in 0.01–100 keV band.**Fig. 2.** MAXI/GSC and SSC $\nu F\nu$ spectra accumulated in the range of A) $t=0.0$ –1.0 d, C) $t=12.0$ –13.0 d, D) $t=18.0$ –19.0 d, E) $t=62.0$ –66.0 d and I) $t=202.0$ –222.0 d, and Swift/XRT snap-shot $\nu F\nu$ spectra taken at, B) $t=1.6$ d, F) $t=97.5$ d, G) $t=113.2$ d and H) $t=165.0$ d.

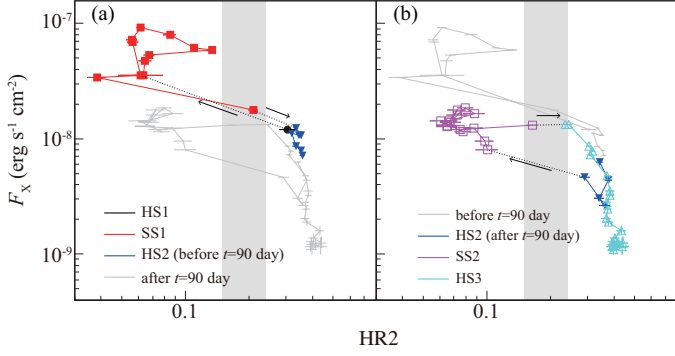


Fig. 4. Hardness Ratio (HR2) vs 0.01-100 keV F_X diagram, in the periods (a) from $t=0$ to 90 d and (b) from 90 to the end. Data corresponding to the periods SS1, SS2, HS1, HS2 and HS3 are shown in red, magenta, black, blue and cyan, respectively. The data points shown in gray color are identical with that of opposite sides. We assumed that soft-to-hard transition occurred at HR ranging from 0.15 to 0.25 (shaded region).

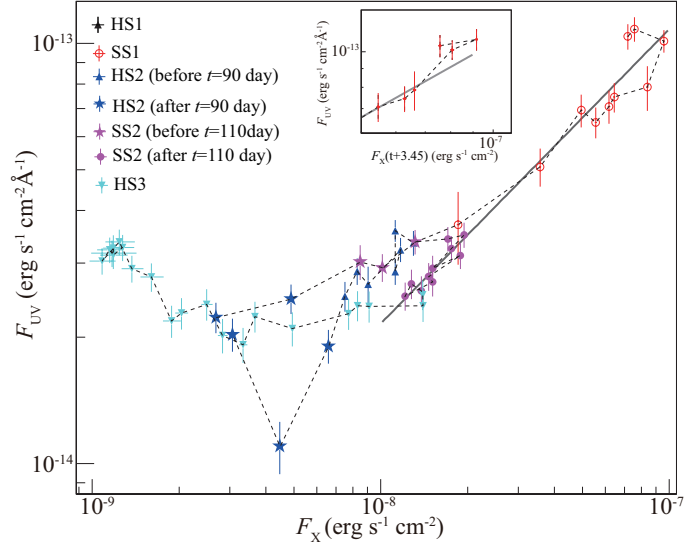


Fig. 6. Scatter plot of F_X versus F_{UV} , with the same color-indexing as figure 4. The data points were connected with a dashed line in the order of time-series. The solid line indicates $F_{UV} \propto F_X^{0.70}$ obtained for SS1 and SS2. Sub figure is modified for a UV-X-ray delay interpolating F_X , solid line is the same as main plot.

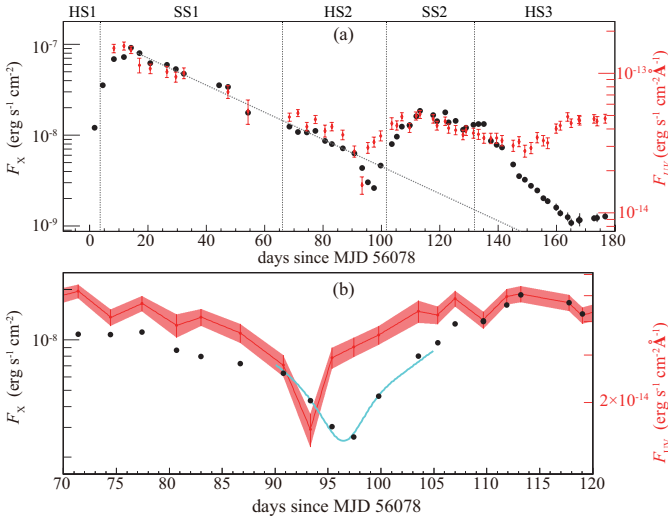


Fig. 5. (a) X-ray and UV light curves until $t=180$ d, black and red plots indicate Swift/XRT 0.01–100 keV F_X derived spectral fits and Swift/UVOT UVM2 flux respectively. The fluxes are corrected for interstellar absorption and extinction with parameters shown in section 3.2, 3.5. (b) Same as above data but zoomed in $t=70$ –120 d, and filled region shows the logarithmic interpolated UVOT data with its statistical error. The best-fit model (see text) is shown in cyan line.

We have overlaid X-ray and UV light curves in figure 5(a). F_X is identical to that indicated in figure 3, and F_{UV} is the same data; but we converted UVM2 Magnitude into extinction-corrected flux. We found that F_X and F_{UV} correlated nicely during exponentially decay phases, that is $t=10$ –90 d and $t=110$ –130 d. The e-folding time of F_X and F_{UV} flux was 30 and 56 days for $t=10$ –90 d, and 37 and 51 days for $t=110$ –130 d, respectively. We obtained e-folding time of F_{UV} to be about twice larger than that of F_X . However, we can find apparent mismatches on $t=90$ –110 d, and after $t=140$ d. We show scatter plots between F_{UV} and F_X in figure 6. Excluding the period $t=90$ –110 d (shown with star points), the relation is approximated by $F_{UV} \propto F_X^{0.70 \pm 0.02}$ in the SS1 and SS.

Figure 5(b) zooms up the light curves around $t=90$ –110 d. We can find the dip with a time difference between F_X and F_{UV} and subsequent F_{UV} excess. In order to estimate the time difference from F_{UV} to F_X on the dip, we perform a model fit. The model is described by a logarithmically interpolated F_{UV} light curve (red region in figure 5(b)) which is convolved with a Gaussian kernel. Using this model, we fitted F_X light curve from $t=90$ to 110 d assuming $F_{UV} \propto F_X^{0.45}$ obtained from the corresponding period of figure 6. Eventually, we obtained a profile of time delay from F_{UV} to F_X to be centered at 3.5 ± 0.2 days and a full-width at half-maximum (FWHM) of $3.8^{+0.8}_{-0.7}$ days. We indicated a best-fit model with a cyan line in 5(b).

3.5. Joint UV and X-ray spectral analysis

In order to investigate origin of the UV emission, we performed Swift/XRT spectral analyses including Swift/UVOT data. We first examined the SS spectra taken at $t=17.0$ d with six UVOT filters. We used a $red\,den \times TBabs \times (diskbb + thcomp)$ model in `xspec` where the *red* model represents the extinction. We found that the UV/optical flux is 2.5-4 times larger

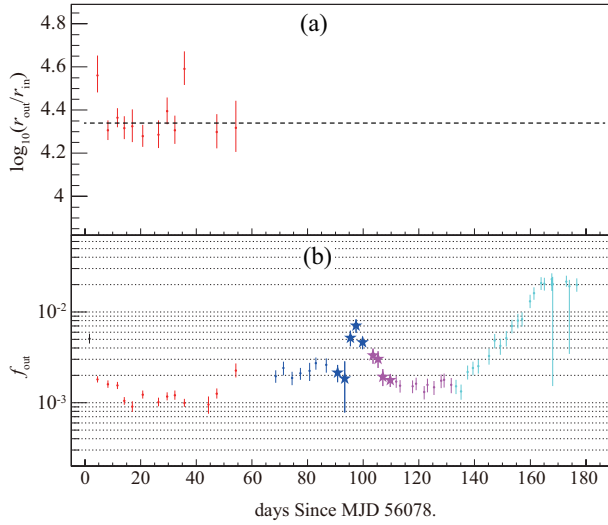


Fig. 8. Change of (a) r_{out} and (b) f_{out} as a function of time obtained with reprocessed disk model. The plot is created in the same manner as figure 6.

than that extrapolated from the MCD. The fitting is far from acceptable level at 3.54 ($\chi^2/\text{d.o.f.} = 1140.1/322$).

Next we employed the *diskir* model (Gierliński et al. 2008) which calculates a reprocessed energy spectrum from an irradiated disk by X-rays from the *diskbb* and *nthcomp* model components. We used a *reddden* × *TBabs* × *diskir* model where we fixed $E(B - V)$ at 0.598, the fraction of the thermalized component f_{in} at 0.1, and a radius of the illuminated disk r_{irr} at 1.1 r_{in} (e.g. Gierliński et al. 2009, Shidatsu et al. 2013).

The fit was acceptable yielding $\chi^2/\text{d.o.f.} = 344.2/320$. Unabsorbed and de-reddened νF_ν spectra of the irradiated disk model and the data are shown in figure 7(a). The model has free parameters of T_{in} , r_{in} , an outer disk radius r_{out} , a luminosity ratio of the Compton tail to the unilluminated (inner) disk L_c/L_d , and a fraction of bolometric flux thermalized in the outer disk f_{out} . The parameters in the X-ray band were almost consistent with those obtained with the *diskbb* model, $T_{\text{in}} = 0.59 \pm 0.01$ keV, $r_{\text{in}} = 170.0^{+4.6}_{-4.5}$ km, $\log_{10}(r_{\text{out}}/r_{\text{in}}) = 4.32^{+0.08}_{-0.07}$, and $f_{\text{out}} = 0.90^{+0.13}_{-0.11} \times 10^{-3}$.

Assuming that the UV-excess fluxes are entirely produced by the disk irradiation, we applied this model for all the Swift observations. Since the spectrum with a single UVOT band data cannot give constraints on r_{out} and f_{out} at the same time. Thus we first analyzed spectra which have 6 UVOT bands allowing both r_{out} and f_{out} to be free. As shown in figure 8(a), $\log_{10}(r_{\text{out}}/r_{\text{in}})$ are found to be constant at ~ 4.33 . Then we fixed r_{out} at this value, and fit the other spectra. The results of f_{out} are shown as a function of time (figure 8 b). The representative spectra and these best-fit parameters are summarized in figures 7 and table 2.

4. Discussions

4.1. Summary of the results

We monitored the entire outburst from MAXI J1910–057 with MAXI and Swift, as the light curves in figure 1. As the

spectrum changed dramatically several times, we separated the periods into the HS1, 2, 3, SS1 and SS2. As described in section 3.2, we analyzed all MAXI stacked spectra and Swift/XRT with a MCD plus a thermal Comptonization model.

MAXI J1910–057 broke out on MJD 56078 ($t = 0$ d). On the first day (HS1), it showed a hard X-ray spectrum, and then it rapidly changed to a soft spectrum (SS1). The X-ray flux reached a maximum at $t = 10$ d. The hard X-ray increased due to an enhancement of Comptonization around $t = 20$ d. We found a secondary peak around $t = 50$ d in 2–6 keV MAXI/GSC light curve, which is a factor of 2 higher than that extrapolated from $t = 10 - 40$ d. However, we consider that it is an induced structure in this energy band due to the hard-to-soft spectral change. Actually, the 0.01–100 keV bolometric flux between $t = 10$ d and 90 d showed a rather steady exponential decay with a time constant of ~ 30 days. We note that Γ remained above 2.0, which is higher than that compared with a typical value in the HS of 1.4–1.7 (Remillard & McClintock 2006). Hence, the HS2 could be characterized as so-called “hard intermediate state”.

A dip structure was found around $t = 95$ d in X-ray flux; it is followed by a bright re-flare (increased by a factor of ~ 10 from the dip) peaking at $t = 113$ day. The X-ray spectrum was confirmed to be the soft state (SS3), meanwhile. Remaining the hard spectrum (HS3), the outburst lasted with a flat tail until $t \sim 230$ d, and then the X-ray flux declined steeply.

4.2. Structure and evolution of the inner accretion disk

The MCD component was significantly detected in both the SS and the HS in the Swift/XRT snapshot spectra. In the SS, the innermost disk radius was almost constant at around 150 km despite a large change in flux over an order of magnitude, while $r_{\text{in}} = 300 - 400$ km was obtained in the HS. We have shown the r_{in} versus disk-flux F_{disk} diagram in figure 9. In the SS, the relation between F_{disk} , T_{in} and r_{in} is known to be $F_{\text{disk}} \propto T_{\text{in}}^4 r_{\text{in}}^2$. During the SS1 and the SS2, F_{disk} tracks on $F_{\text{disk}} \propto T_{\text{in}}^4$. However, it clearly deviates in the HS2 and the first half of the HS3, implying the truncation of the inner disk (Zdziarski et al. 1998).

Next, we estimate the mass of the central star, firstly assumed to be a black hole, from the inner disk radius. If a color correction factor κ has little dependence of r (Shimura & Takahara 1995), the innermost radius R_{in} in the standard accretion disk model can be approximately expressed by $R_{\text{in}} = \kappa^2 \xi r_{\text{in}}$, where ξ is a correction factor for a maximal flux or temperature radius. Though both κ and ξ have some uncertainties (e.g., see Davis et al. 2005 for κ , and see Dotani et al. 1998 for ξ), we take $\kappa = 1.7$ and $\xi = 0.412$ (Kubota et al. 1998) to directly compare with our previous results (Nakahira et al. 2012, Yamaoka et al. 2012, Morihana et al. 2013). By adopting the SS2 averaged radius of 138.0 ± 9.0 km as ISCO, the mass for a non-spinning black hole is estimated as

$$M_{\text{BH}} = \frac{c^2 R_{\text{in}}}{6G} = 18.5 \pm 1.2 \left(\frac{D}{10 \text{ kpc}} \right) (\cos i)^{-\frac{1}{2}} M_{\odot}. \quad (2)$$

with a source distance in unit of 10 kpc and an inclination angle from our line-of-sight i . Since no dip or eclipse feature was observed, we assume $i = 0 - 60^\circ$. Thus, the distance and mass is constrained to the shadowed region in figure 10. Following

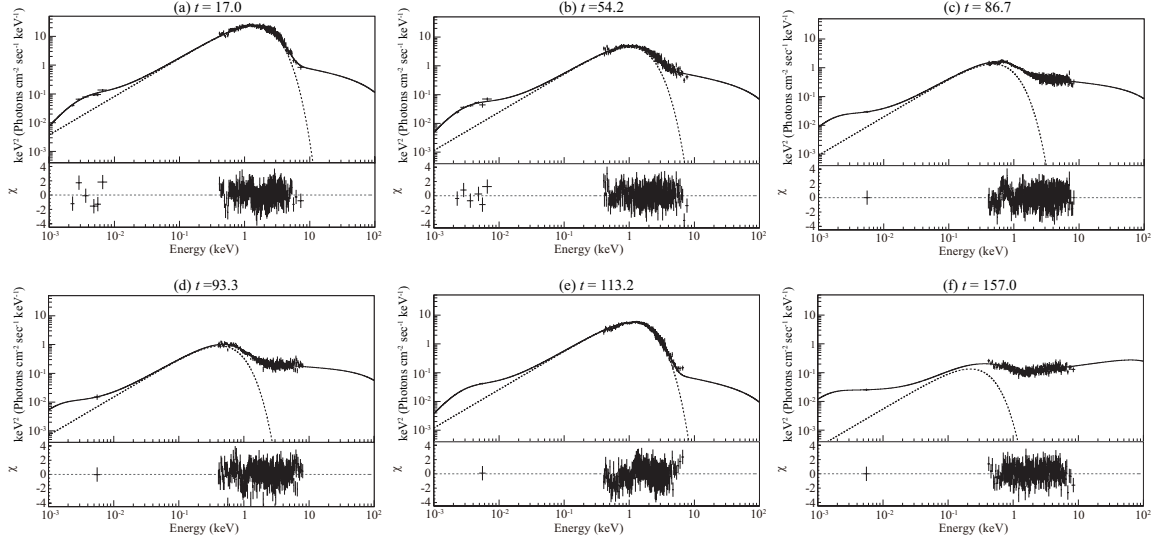


Fig. 7. UV and X-ray $\nu F\nu$ spectra obtained by Swift UVOT and XRT, respectively, at $t = 17.0$ d, 54.2 d, 86.7 d, 86.7 d, 93.3 d, 113.2 d, and 157.0 d. Each upper panel shows observed and model spectra corrected for interstellar absorption and extinction. The solid line indicates a total reprocessed disk spectrum, and the dashed line shows an intrinsic disk spectrum. Bottom panels represent residuals between the UV and X-ray data and the reprocessed model.

Table 2. Best-fit model parameters obtained from a reprocessed model with Swift/XRT and UVOT spectra.

Time*	T_{in} (keV)	r_{in}^{\dagger} (km)	Γ	F_c/F_d^{\ddagger}	f_{out}^{\S} $\times 10^{-3}$	$\log_{10}(r_{\text{out}}/r_{\text{in}})^{\parallel}$	$\chi^2 / \text{d.o.f.}$	$f_{\text{UV}}^{\text{obs}} / f_{\text{UV}}^{\text{MCD}\#}$
17.0	0.59 ± 0.01	$170.0^{+4.6}_{-4.5}$	2.40 (fixed)	0.06 ± 0.01	$0.90^{+0.13}_{-0.11}$	$4.32^{+0.08}_{-0.07}$	343.8 / 320	2.56 ± 0.31
54.2	0.42 ± 0.01	$148.0^{+4.8}_{-4.6}$	2.40 (fixed)	0.23 ± 0.01	$2.25^{+0.46}_{-0.35}$	$4.32^{+0.13}_{-0.11}$	340.4 / 336	3.86 ± 0.77
86.7	0.20 ± 0.01	349^{+20}_{-19}	2.22 ± 0.05	0.64 ± 0.02	2.60 ± 0.47	4.33 (fixed)	444.9 / 431	3.52 ± 0.29
93.3	0.18 ± 0.01	354^{+26}_{-24}	2.14 ± 0.07	0.51 ± 0.03	$1.84^{+1.01}_{-1.06}$	4.33 (fixed)	411.8 / 323	2.31 ± 0.48
113.2	0.47 ± 0.01	128.2 ± 2.2	2.40 (fixed)	0.02 ± 0.01	1.53 ± 0.24	4.33 (fixed)	388.1 / 324	3.55 ± 0.25
157.0	0.09 ± 0.01	517^{+71}_{-59}	1.72 ± 0.05	$4.04^{+1.88}_{-1.05}$	$8.35^{+1.60}_{-1.47}$	4.33 (fixed)	252.2 / 248	17.76 ± 1.58

* Elapsed days since MJD=56078.0

† D=10.0 kpc and $i = 0^\circ$ (face-on) are assumed.

‡ ratio of luminosity in the Compton tail to that of the unilluminated disk

§ fraction of bolometric flux which is thermalized in the outer disk

$^{\parallel}$ \log_{10} of the outer disk radius in terms of the inner disk radius

$^{\#}$ ratio of observed UVM2 band flux to that calculated from MCD

* fraction of luminosity in the Compton tail which is thermalized in the inner disk is fixed at 0.1

†† radius of the Compton illuminated disk in terms of the inner disk radius is fixed at 1.1

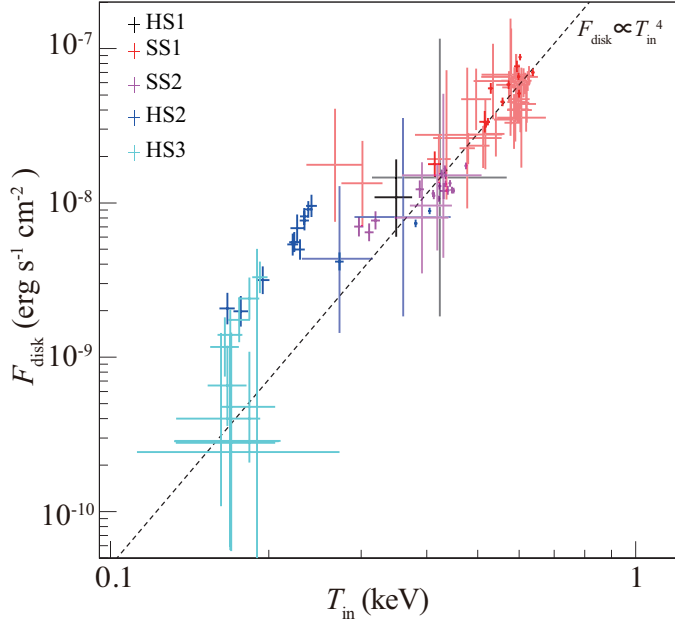


Fig. 9. The correlation between T_{in} and Comptonization-corrected disk flux, data points in each periods are shown in the same colors as in figure 4 and 6. The data taken by Swift/XRT are shown in solid colors, and those by MAXI/GSC in faint colors. The dashed line indicates $F_{\text{disk}} \propto T_{\text{in}}^4$.

Nakahira et al. (2012) and Yamaoka et al. (2012), we derive further constraints using an empirical correlation offered by Maccarone (2003) that the soft-to-hard spectral state transition occurs between 1 to 4 % of Eddington luminosity. If we assume that the soft-to-hard transition fluxes of $1.28\text{--}2.33 \times 10^{-8} \text{ erg cm}^{-2} \text{ s}^{-1}$ obtained in section 3.2 lie in this L_{edd} range, then the hatched region in figure 10 can be derived, and the minimum and maximum masses are obtained as $2.9 M_{\odot}$ for $D = 1.7 \text{ kpc}$ and $12.9 M_{\odot}$ for $D = 5.3 \text{ kpc}$, respectively. The lower limit close to $3 M_{\odot}$ is consistent with a picture that the central star is a black hole as assumed in the mass derivation. A further detailed estimation of the mass fully taking account of the general relativistic effects is out of the scope of this paper.

We note that r_{in} used in the SS2 is slightly different from that in the SS1, which might be due to that Compton scattering above the disk is partially expressed by the *nthcomp* model, not the hardening factor κ . We also note that a larger radius $r_{\text{in}} \simeq 200 \text{ km}$ was obtained on $t \sim 140 \text{ d}$, when *XMM-Newton* observation was carried out (Reis et al. 2013). The larger radius than that in the SS implies the truncation of the optically thick disk in that state, rather than an intrinsically large innermost radius of a retrogradely spinning black hole (Reis et al. 2013).

4.3. Origin of UV and X-ray Dip and Re-flaring

The “fast-rise and exponential-decay” type of outbursts is well explained by a sudden and temporary increase in mass accretion induced, for instance, by a disk thermal instability (Mineshige & Wheeler 1994, Cannizzo et al. 1994). During the steady-decline phases in $t = 10\text{--}90 \text{ d}$ and $110\text{--}140 \text{ d}$, both the F_{X} and F_{UV} light curves of MAXI J1910–057 exhibited

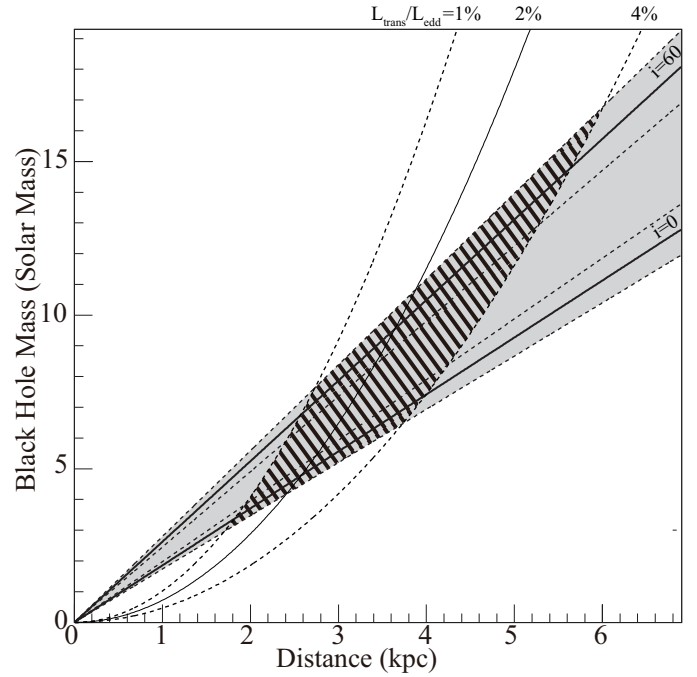


Fig. 10. Observational constraints on the distance-mass diagram. The shadowed region comes from the innermost radius derived from X-ray spectral analysis assuming an inclination angle of 0 to 60 degree, and the solid lines with the two dashed lines in the region indicate the best-fit parameters and their errors when $i = 0^\circ$ and 60° . The hatched area is derived by further assuming the empirical relation that the soft to hard transition occurs at 1–4% L_{edd} .

exponential decays (figure 5). Behaviors of the curves around $t = 90\text{--}110 \text{ d}$ and after $t = 140 \text{ d}$ are, however, different. In $t = 90\text{--}110 \text{ d}$, both the curves are characterized by the sharp drop, and F_{X} lags behind F_{UV} . We computed the time delay and the profile focusing on the sharp drop in section 3.4. By employing the convolution model with a Gaussian kernel, we obtained the lag time of 3.5 ± 0.2 days and the diffusion time of $3.8^{+0.8}_{-0.7}$ days (FWHM). The lag time is consistent with 4.06 ± 0.71 days obtained by Degenaar et al. (2014) who used the same Swift UVOT and XRT data. We also note that the hysteresis in the right-top of figure 6 suggests the same delay in the early part of the outburst.

What does the dip mean? Degenaar et al. (2014) extensively argued the cause of the dip in connection with jets and state transitions. Here, we also discuss a possibility of non-steady accretion flow. In the optically thick accretions disk, the disk temperature T decreases outward as $T \propto r^{-3/4}$. Assuming most photons having energy E come from the region with temperature $T (\sim E/k)$ according to the Wien’s displacement law, we observe photons with E from the radius at $r \propto E^{-4/3}$. Thus, it is possible that the observed energy and time dependent dip is caused by a low mass-accretion-rate (dark ring) region taking place at an outer part of the disk and drifting inward. From the SED at $t = 93.3 \text{ d}$ (figure 7(d)), a ratio of the X-ray-flux-peak energy E_{X} to the UVOT (filter) central energy (2246 \AA) E_{UV} , $E_{\text{X}}/E_{\text{UV}}$, is ~ 100 . Thus, the radius of the UV emission region r_{UV} can be roughly estimated as

$r_{UV} \simeq (E_{UV}/E_X)^{-4/3} r_{in} \sim 500 r_{in} \sim 3000 r_s$. Here we assume that X-rays with E_X mostly come from near r_{in} , and use $r_{in} \simeq 2R_{in} (\simeq 6 r_s)$ from Tables 1 or 2. We ignore the effect of the irradiation here.

This UV radiation radius is comparable to the radius estimated from the viscous time scale for 6 days of Optical-to-X-rays time lags (Degenaar et al. 2014) though the viscous time scale has the uncertainty of one or two orders of magnitude. It is interesting to note that the viscous time scale is also known as the (radial) *drift* time scale (Lightman 1974) and the *diffusion* time scale (Frank et al. 2002). Thus, the time lags (~ 3.5 days) and the comparable diffusion time (~ 3.8 days) we obtained are consistent with the above picture.

The dip might be also associated with the bright 3rd maximum around $t \sim 120$ d because a similar X-ray flux drop before the 3rd maximum was also observed in A 0620-00 (Kaluzienski et al. 1977). An apparent flux excess over the exponential decay implies enhancement of a mass-accretion rate by an extra mass input to the disk. If the accretion rate decreases at an outer part of the disk, a transition into a cool (~ 6000 K) branch of a Hydrogen neutral state sets in (Meyer & Meyer-Hofmeister 1981). In the cool branch, the viscosity is so small that the mass accretion once stagnates there. This might result in the dark ring region just inside it. The transition also causes a vertical shrink of the outer disk, allowing irradiation to the companion star. This gives rise to an additional mass transfer to the accretion disk invoked by mass transfer instability (e.g., Chen et al. 1993), and the disk backs to a hot branch of a Hydrogen ionized state.

Finally, we also note that the UV dip might be partially triggered by the transition because the temperature of the hot branch is about 10^4 K, of which the peak energy is around 3.4 eV. As pointed out by Degenaar et al. (2014), however, these scenarios can not explain the sudden nIR color change (bluer) observed with the sharp drop in UVs.

After $t = 140$ d, F_X and F_{UV} changed asymmetrically. From the fits to the Swift/XRT plus UVOT spectra with the reprocessed disk model (figure 7), a reprocessed fraction can be considered to be increasing with time. In the present data, however, we cannot rule out other possibilities. The UV component might be due to other components such as a jet and/or an inner hot accretion flow (e.g., Yuan et al. 2005), and the soft X-ray component also to an “additional variable component” (Chiang et al. 2010), e.g., X-ray shots with a soft X-ray spectrum and associated optical jets (Negoro et al. 1994, Malzac et al. 2003), instead of the Keplerian (less variable) disk component.

5. Conclusion

We have presented light curves and spectral results of the entire outburst using data obtained by MAXI and Swift of the X-ray nova MAXIJ1910–057. The light curve was a fast-rise and exponential-decay type suggesting a disk thermal instability outburst. As well as past observations of X-ray novae, the broad third maximum was detected. The X-ray spectral state around the main peak and the third maximum were confirmed to be the SS. Since the innermost radius kept roughly constant in the SS, and the relation between disk flux and temperature was approximated by $F_{disk} \propto T_{in}^4$, we interpreted the radius as

an ISCO. The innermost radius became larger in the hard state. This suggests that the accretion disk was truncated. The X-ray fluxes of two series of “hard-to-soft” transitions agreed within a factor of two. By assuming that the “hard-to-soft” transitions occurs 1–4% of Eddington luminosity, the lower limit of the black hole mass is estimated to be $2.9 M_\odot$.

We also studied the relation between UV data in combination with X-ray data. Their joint spectral analysis revealed that the UV emission is composed of direct MCD emission and its reprocessed emission from outer disk. Using the sharp drop found in both the light curves, the profile of time delay is approximated with a Gaussian profile centering at 3.5 days and the width of 3.8 days FWHM. We conclude that the time difference reflects changing mass accretion rate accreting inward, which possibly caused by local instability.

This research has made use of MAXI data provided by RIKEN, JAXA and the MAXI team. We also thank the Swift team for their observation. This work made use of data supplied by the UK Swift Science Data Centre at the University of Leicester.

References

- Burrows, D. N., et al. 2005., Space Sci. Rev.120, 165
- Barthelmy, S. D., et al. 2005., Space Sci. Rev.120, 143
- Cannizzo, J. K., Wheeler, J. C., & Ghosh, P., 1985, in Cataclysmic Variables and Low-Mass X-ray Binaries, ed. D. Q. Lamb & J. Patterson (Dordrecht: Ridell), 307
- Chen, W., Livio, M., & Gehrels, N., 1993, ApJ, 408, L5
- Chen, W., Shrader, C. R., & Libio, M., 1997, ApJ, 491, 312
- Chiang, C. Y., et al., 2010, MNRAS, 403, 1102
- Degenaar, N., Maitra, D., Cackett, E., M. et al., 2014, ApJ, 784, 122
- Ebisawa, K., et al., 1994, PASJ, 46, 375
- Davis, S.W., et al., 2005, ApJ, 621, 372
- Dotani, T., et al., 1997, ApJ, 485, L87
- Evans, P. A., et al., 2009, MNRAS, 397, 1177
- Frank, J., King, A., & Raine, D., 2002, in Accretion Power in Astrophysics (third edition), ed. R.F. Carswell, D.N.C. Lin and J.E. Pringle (Cambridge University Press)
- Gierliński, M., Done, C. & Page, K. 2008, MNRAS, 388, 753
- Gierliński, M., Done, C. & Page, K. 2009, MNRAS, 392, 1106
- Güver, T. & Özel, F., 2009, MNRAS, 400, 2050
- Hameury, J. M., King, A. E., & Lasota, J. P., 1986, A&A, 162, 71
- Harmon, A. et al., 1992, IAU Circ., 5584
- Homan, J. & Belloni, T. 2005, Ap&SS, 300,107
- Kaluzienski, L. J., Jpl, S. S., Boldt, E. A., & Serlemitsosm P. J., 1977, ApJ, 212, 203
- Kennea, J. A., et al., 2012, The Astronomer’s Telegram, #4145
- Kimura, M., et al., 2012, The Astronomer’s Telegram, #4198
- Krimm, H. A., et al., 2012, The Astronomer’s Telegram, #4139
- Krimm, H. A., et al., 2013, ApJS, 209,14
- Kubota, A., et al., 1998, PASJ, 50, 667
- Kubota, A., & Makishima, K. 2004, ApJ, 601, 428
- Lightman, A. P., 1974, ApJ, 194, 419
- Maccarone, T J., 2003, A&A, 409, 697
- Makishima, K., et al., 2008, PASJ, 60, 585
- Malzac, J., et al., 2003, A&A, 407, 335
- Matsuoka, M., et al., 2009, PASJ, 61, 999
- McClintock, J. E., Remillard, R. E., at al., 2009, ApJ, 698, 1398
- Meyer, F., & Meyer-Hofmeister, E., 1981, A&A, 104, L10
- Mihara, T., Nakajima, M., Sugizaki, M., et al., 2011, PASJ, 63, S623
- Mineshige, S., Wheeler, J. C., 1989., ApJ, 343, 241

- Mitsuda, K., et al., 1984, PASJ, 36, 741
Morihana, K., et al., 2013, PASJ, 65, L10
Nakahira, S., et al., 2010, PASJ, 62, L28
Nakahira, S., et al., 2012, PASJ, 64, 13
Nakahira, S., et al., 2012, The Astronomer's Telegram, 4273
Nakahira, S., et al., 2012, Journal of Space Science Informatics Japan, 2, 29
Negoro, H., Miyamoto, S., & Kitamoto, S., 1994, ApJ, 423, L127
Negoro et al., 2012, Astronomical Society of the Pacific Conference Series, Vol. 461, Astronomical Data Analysis Software and Systems XXI, ed.
Raum A., Greiner, J., Schady, P., 2012, The Astronomer's Telegram, #4143
Reis, R. C., Reynolds, M. T., Miller, J. M. et al., 2013, ApJ, 778, 155
Remillard, R. E. & McClintock, J. E., 2006, ARA&A, 44, 49
Roming, P. W. A., et al. 2005, Space Sci. Rev., 120, 95
Savage B. D., & Mathis J. S., 1979, ARA&A, 17, 73
Shakura, N. I., & Sunyaev, R. A. 1973, A&A, 24, 337
Sunyaev, R. A., Trümper, J., 2013, ApJ, 779, 26
Shidatsu, M., et al., 2013, ApJ, 779, 26
Shimura, T., & Takahara, F., 1995, ApJ, 445, 780
Sugizaki, M., Mihara, T., et al., 2011, PASJ, 63, S635
Tanaka, Y., & Shibazaki, N., 1996, ARA&A, 34, 607
Tomida, H., et al., 2011, PASJ, 63, 397
Tsunemi, H., Kitamoto, S., Okamura, S., & Roussel-Dupré, D., ApJ, 337, L81
Tsunemi, H., et al., 2010, PASJ, 62, 1371
Usui, R., et al., 2012, The Astronomer's Telegram, #4140
Wilms, J., Allen, A., & McCray, R., 2000, ApJ, 42, 914
Yamaoka, K. et al., 2012, PASJ, 64, 32
Yuan, F., Cui, W., & Narayan, R., 2005, ApJ, 620, 905
Zdziarski, A. A., et al., 1995, MNRAS, 301, 435